

AN OVERDENSITY OF *I*-DROPOUTS AMONG A POPULATION OF EXCESS FIELD OBJECTS IN THE VIRGO CLUSTER¹

HAOJING YAN², NIMISH P. HATHI³ & ROGIER A. WINDHORST⁴

Draft version January 4, 2019

ABSTRACT

Using a set of deep imaging data obtained by the Advanced Camera for Surveys (ACS) on the *Hubble Space Telescope* (*HST*) shortly after its deployment, Yan, Windhorst & Cohen (2003) found a large number of F775W-band dropouts (*i*-dropouts), which are consistent with being galaxies at $z \approx 6$. The surface density of *i*-dropouts thus derived, however, is an order of magnitude higher than those subsequent studies found in other deep ACS fields, including the *Hubble* Ultra-Deep Field (HUDF). Here we revisit this problem, using both the existing data and the new data obtained for this purpose. We confirm that the large overdensity of *i*-dropouts does exist in this field, and that their optical-to-IR colors are similar to those in the HUDF. However, we have discovered that the *i*-dropout overdensity is accompanied with an even larger excess of faint field objects in this region and its vicinity. This large excess of field objects is most likely caused by the fact that we have resolved the faint diffuse light extending from an interacting galaxy pair in the Virgo Cluster, M60/NGC4647, which lies several arcminutes away from the region where the excess is found. The integrated light from the excess is a few percent of the luminosity of the galaxy pair. We argue that this excess population is most likely tidal “debris” and/or halo stars related to the galaxy pair rather than to the Virgo Cluster in general. The *i*-dropouts in this field are within the magnitude range where this excess of field objects occurs. The spatial distribution of the *i*-dropouts seems to follow the same gradient as the excess field population. This excess population is also red in color, and the red wing of its color distribution continuously extends to the regime where the *i*-dropouts reside. While we still cannot completely rule out the possibility that the overdensity of *i*-dropouts might be a genuine large-scale structure of galaxies at $z \approx 6$, we prefer the interpretation that most of them are part of the excess stellar population related to M60/NGC4647. Future spectroscopic work will be needed to unambiguously identify the nature of this *i*-dropout overdensity.

Subject headings: galaxies: high-redshift — galaxies: halos — galaxies: interactions — stars: AGB and post-AGB

1. INTRODUCTION

The so-called “Lyman-break” technique (Steidel & Hamilton 1992) is now widely used to select galaxies at high redshifts. This method relies on multi-band imaging to identify the characteristic discontinuity — the *Lyman-break* — in the spectral energy distributions (SED) of high-redshift galaxies, which is largely caused by the Lyman-limit and *Ly α* absorptions of intervening neutral hydrogen along the sightlines to such galaxies (e.g., Madau 1995). The technique requires imaging in at least two passbands, one to the blue side of the break and the other to the red side. Lyman-break makes high-redshift galaxies much fainter in the blue band than in the red one, or in other words, it makes them seem to “drop-out” from the blue band. For this reason, this method is also known as the “drop-out” selection, and the candidates found in this way are usually referred to as “dropouts”.

As its first application in the $z \approx 6$ regime, Yan, Windhorst & Cohen (2003; hereafter YWC03) used this technique in a deep field observed by the Advanced Camera for Surveys (ACS; Ford et al. 2003) in the default pure parallel mode (Sparks et al. 2001) soon after its deployment on-board the Hubble Space Telescope (*HST*). In this redshift range, Lyman-break occurs at around 8512Å in observer’s frame (restframe 1216Å), which is well targeted by the F775W and F850LP filters through which this deep parallel field was imaged. YWC03 found a large number of F775W-band dropouts, and argued that the vast majority of them were very likely galaxies at $z \approx 6$.

The number density of $z \approx 6$ galaxies inferred from YWC03, however, seem to be much higher than those in other deep ACS fields (e.g., Bouwens et al. 2003; Stanway, Bunker & McMahon 2003; Dickinson et al. 2004; Bouwens et al. 2004; Bunker et al. 2004; Yan & Windhorst 2004, hereafter YW04). While the cosmic variance could result in significant fluctuation in the number density (e.g., Somerville et al. 2004; Bouwens et al. 2004), it cannot account for the large difference between the result of YWC03 and those of others. As the true number density of galaxies at $z \approx 6$ is closely related to a series of important cosmological questions (e.g., the formation of early galaxies; the reionization history of the universe; etc.), it is prudent to closely examine the cause of the observed difference.

¹ Based on observations made with the NASA/ESA Hubble Space Telescope, obtained at the Space Telescope Science Institute, which is operated by the Association of Universities for Research in Astronomy, Inc., under NASA contract NAS 5-26555. These observations are associated with programs #9780, 9488, 9575, 9584, and 9984

² The Observatories of the Carnegie Institution of Washington, 813 Santa Barbara Street, Pasadena, CA 91101; yhj@ociw.edu

³ Department of Physics, Arizona State University, Tempe, AZ 85287

⁴ School of Earth & Space Exploration, Arizona State University, Tempe, AZ 85287

In this paper, we present new results that shed light to the nature of this overdensity. We first describe the existing and new *HST* observations in §2 and the data reduction in §3. The overdensity of F775W-band dropouts in YWC03 is scrutinized in §4, and a new interpretation is given in §5. We conclude with a summary in §6. For simplicity, we refer to the *HST* F475W, F775W, F850LP, F110W, and F160W passbands as g_{475} , i_{775} , z_{850} , J_{110} , and H_{160} , respectively. The F775W-band dropouts are then referred to as i -dropouts. The magnitudes are in AB system. All coordinates quoted are in J2000. The following cosmological parameters from the first-year Wilkinson Microwave Anisotropy Probe (WMAP) results in Spergal et al. (2003) are adopted: $(\Omega_M, \Omega_\Lambda, H_0) = (0.27, 0.73, 71)$. Using the three-year WMAP results (Spergal et al. 2007) would not change any of our results.

2. OBSERVATIONS

In addition to the ACS parallel field discussed in YWC03 (hereafter referred to as “Par1”), we have acquired two sets of new observations to help tackle the question at hand. To follow-up a subset of the i -dropouts found in YWC03, two regions in Par1 were imaged by the Near Infrared Camera and Multi-Object Spectrometer (NICMOS) Camera 3 (NIC3). During the course of these NIC3 observations, the ACS instrument was working in parallel, which resulted in a new ACS parallel field (hereafter referred to as “Par2”) that is several arcminutes away from the original one. The layout of these two ACS fields are shown in Fig. 1. Note that they are in the general direction of the Virgo Cluster. We describe all these observations below.

2.1. ACS parallel observations of Par1

The center of Par1 is at $RA = 12^h 43^m 32^s$, $Dec = 11^\circ 40' 32''$. The ACS data were taken during *HST* Cycle 11 soon after the instrument was installed in March, 2002. In fact, the observations spanned from April 28 to June 19, 2002, and were acquired during the execution of the Guest Observer (GO) program ID 9043 (PI. Tonry), when it was using the Wide-Field Planetary Camera 2 (WFPC2) as the primary instrument to image NGC4647, which is a member of the Virgo Cluster. Only i_{775} and z_{850} filters were used for these ACS parallels. In total, 15 images were taken in i_{775} and 27 images were taken in z_{850} . The total exposure time in these two bands is 2.65 hours and 4.28 hours, respectively.

2.2. NIC3 observations in Par1

Our NIC3 observations of Par1 were carried out as a GO program (PID 9780) in *HST* Cycle-12. Two regions in Par1, designated as fields “Sub1” and “Sub2”, were observed in J_{110} and H_{160} . Due to an unfortunate system glitch that caused NICMOS enter a short safing-mode period in early August 2003, our program missed its originally planned visit windows, and its execution had to stretch from January to December 2004 through rescheduled visits.

For each field, the observations were done at 15 dithering positions in J_{110} and 25 positions in H_{160} . The observation mode was MULTIACCUM with SPARS64 sequence. The exposure time at each dithering position is

512 seconds, resulting in a total integration time of 2.13 hours in J_{110} and 3.56 hours in H_{160} , respectively.

2.3. ACS parallel observations of Par2

While our NIC3 program was not executed in August 2003 as originally scheduled, part of its ACS parallel observations were still automatically carried out on August 5 and 6, 2003 as planned in default. This resulted in Par2, which is about $8'$ to the north of Par1. The field center is $RA = 12^h 43^m 30^s$, $Dec = 11^\circ 49' 21^s$. In total, 5 images in z_{850} , 12 images in i_{775} and 6 images in g_{475} were taken in this field, giving a net exposure time of 1.00, 1.80 and 0.89 hours in these three bands, respectively.

3. DATA REDUCTION AND PHOTOMETRY

In this section, we discuss the data reduction and photometry of all relevant *HST* images.

3.1. ACS data reduction

When the YWC03 paper was written (September 2002), the *HST* “On-the-Fly Reprocessing” (OTFR) calibration pipeline could only process ACS data up to the step of geometric distortion correction. The *Multidrizzle* package (Koekemoer et al. 2002), now a standard tool for mosaicing ACS images using the drizzle algorithm (Fruchter & Hook 2002), was then not yet well known and tested. Therefore, the ACS mosaics of Par1 used in YWC03 were created by stacking the flat-fielded, distortion-corrected images utilizing the well-tested *IM-COMBINE* task of IRAF that had been used by the community for decades.

For this current study, the ACS data of Par1 were retrieved again from the *HST* data archive. In so doing, the requested data were automatically reprocessed by the OTFR pipeline using the best reference files (bias, dark current, flat field, etc.) currently available. New mosaics were then made from these reprocessed images by using the now-fully-matured *Multidrizzle* routine as available in STSDAS under PyRAF. The reduction of the Par2 ACS data followed the same procedure.

Some ACS/WFC OTFR-processed images are known to show a quadrant-to-quadrant “jump” in background because of the varying residual bias levels in the four ACS/WFC readout amplifiers (Pavlovsky et al. 2005). While this bias offset is minimal in the data of Par2 ($\sim 0.1e^-$ level), it is obvious in most of the Par1 images ($\sim 10e^-$ level). Although such “jumps” do not have significant impact on the photometry of compact sources in general, they do affect the sources that are close to quadrant boundaries. Therefore, before stacking the Par1 data, such jumps were removed by subtracting the background from each quadrant using our home-grown routines. The quadrant offsets were reduced to $\sim 1e^-$ level after this process.

The final mosaics were created following the standard drizzling procedures implemented in *Multidrizzle*, and were normalized to unit exposure time (count per second). A square kernel was used in drizzling, and the linear size of drop was set to 0.9 (the “final_pixfrac” parameter of *Multidrizzle*). To get a finer spatial resolution, the drizzle scale (the “final_scale” parameter) was set to 0.6, which resulted in an output pixel scale of $0.03''/\text{pixel}$.

For each field, the output mosaics in different passbands were all registered to the same reference position in the process. The absolute astrometry of the final mosaics was calibrated by using the compact objects visible in the Digital Sky Survey images.

In order to provide a reference frame for Par1 NIC3 data reduction, another version of Par1 ACS mosaics was also created by setting drizzle scale to 1.0, i.e., preserving the native pixel scale (0.05"/pixel) of the ACS/WFC. We will refer to these lower-resolution mosaics and the higher-resolution ones mentioned above as “LOWRS” and “HIGHRS” ACS mosaics, respectively. They each serve different purposes in the analysis process.

As the original pixels were resampled during drizzling (and during geometric distortion correction as well), the final mosaics all have correlated pixel noise. The signal-to-noise ratio (S/N) of a given object derived directly from the final mosaic would therefore be overestimated, and hence its photometric error would be underestimated. We used a routine, kindly provided to one of us (HY) by Dr. Mark Dickinson, to calculate the correlation amplitude and hence to calculate proper statistical error associated with each pixel. The error map (so-called “RMS” map) derived in this way are widely used, e.g., in the data analysis of GOODS (e.g., Dickinson et al. 2004).

3.2. NIC3 data reduction

All data obtained by NICMOS show a number of persistent anomalies that cannot currently be handled by the OTFR pipeline. Therefore, the OTFR-processed NIC3 data of Sub1 and Sub2 fetched from the archive were further reduced before stacking.

An additional count-rate and wavelength dependent non-linearity of NICMOS was recently identified by the STScI NICMOS team (NICMOS Instrument Science Reports 2006-001, 002 and 003; see also <http://www.stsci.edu/hst/nicmos/performance/anomalies/nonlinearity.html>). This non-linearity was removed from the data by using the routine provided by the team.

The quadrant bias of NICMOS also has a stochastic behavior similar to what described above for ACS. As a result, a bias-corrected NICMOS image using the standard bias reference file usually show “pedestals” from quadrant to quadrant. Such pedestals were removed by using the *PESKY* task included in the STSDAS package.

All OTFR-processed NIC3 data have a persistent, additive pattern across entire field. This pattern is different in different passbands, but is rather stable with respect to time. To remove this pattern, a “pattern image” in each band was first created by stacking all the pedestal-corrected images in this band. The pattern image was then subtracted from each individual image.

After all the above steps, the individual images were combined using the series of drizzle tasks included in the *DITHER* package of STSDAS in IRAF. Each input science image was weighted by a weight image calculated from its associated error array stored in the [ERR,2] extension of the OTFR-processed image. For the purpose of matched-aperture photometry that will be discussed below, the LOWRS Par1 ACS z_{850} -band mosaic was binned in 2×2 and then used as the reference. The NIC3 images were all mapped (i.e., rotated and registered) to this binned ACS image during the drizzling

process. The drizzle scale was set to 0.5, which resulted in a final resolution of 0.10"/pixel, i.e., the same as the binned LOWRS ACS image. The final mosaics were normalized to unit exposure time as well.

The associated RMS maps of all these NIC3 mosaics were derived in the way similar to what described above for the ACS mosaics.

3.3. ACS source detection

As compared to the ACS mosaics used in YWC03, the new mosaics created through the improved reduction process (see §3.1) are of much higher quality, and hence we can push to a significantly lower threshold for source detection.

SExtractor (Bertin & Arnouts 1996) was run on the HIGHRS mosaics in dual-image mode to extract source catalogs for both Par1 and Par2. “MAG_AUTO” magnitudes were used to best approach the total magnitudes. A number of source catalogs were obtained for different purposes. The i_{775} -band and z_{850} -band mosaics were used alternatively as the detection images to perform “matched-aperture photometry”, i.e., measuring the magnitudes of a given source in different bands through the same aperture defined by its appearance on the detection image. We will refer to these catalogs as “ i_{775} -based” and “ z_{850} -based” ACS catalogs, respectively. Source detection was performed at the threshold of 0.8σ , using a 5×5 Gaussian filter with a full-width-at-half-maximum (FWHM) of 2.5 pixels. A minimum number of 4 connected pixels were required for a source to be included.

As Par1 was observed in parallel mode during the very early stage of ACS, the data were all taken at a high gain setting of $4.0 e^-/\text{ADU}$, probably for safety reason (i.e., avoiding saturation). In order to make the zeropoints derived at a gain setting of $1.0 e^-/\text{ADU}$ universally applicable, the ACS OTFR pipeline multiplies the flat-field reference file by the gain of the object image before flat-field correction. In the end, an OTFR-processed ACS image always has an effective gain of $1.0 e^-/\text{ADU}$. When YWC03 was written, unfortunately, the authors were not aware of this — at that time poorly-documented — step in the OTFR processing, and made a redundant correction for the gain by adding $2.5 \times \log_{10}(4.0) = 1.505$ to the zeropoints. As a result, while the candidate selection in YWC03 remains valid, all magnitudes reported in that paper were too faint by 1.505 mag. This error has been reported in a footnote in YW04.

In this current study, the zeropoints published in the latest ACS handbook were used; namely, 26.068, 25.654 and 24.862 mag for g_{475} , i_{775} and z_{850} , respectively. The 3σ limits within a circular aperture of $0.1''$ in radius are 29.1 and 28.3 mag in i_{775} and z_{850} in Par1, and 28.9, 28.7 and 27.9 mag in g_{475} , i_{775} and z_{850} in Par2, respectively.

3.4. NIC3 source detection

Photometry of Sub1 and Sub2 NIC3 mosaics in Par1 was also done in dual-image mode, using J_{110} and H_{160} mosaics alternatively as the detection images. Similarly, we will refer to these catalogs as “ J_{110} -based” and “ H_{160} -based” catalogs, respectively. The detection filter was a 5×5 Gaussian filter with a FWHM of 3 pixels, the detection threshold was set to 0.4σ , and a minimum of

2 connecting pixels were required. Again, MAG_AUTO magnitudes were adopted. As the magnitude zeropoints provided by the OTFR pipeline were no longer valid after the non-linearity correction described in §3.2, we followed the recipe given by the NICMOS team to derive the zeropoints as 23.242 and 23.139 mag in J_{110} and H_{160} , respectively.

During this process, ACS magnitudes of the NIC3 sources were also extracted in order to properly measure their ACS-to-NICMOS colors for later analysis. As the NIC3 mosaics were created by registering to the reference frame defined by the 2×2 binned LOWRS ACS mosaics, matched-aperture photometry between NIC3 and ACS passbands was fairly straightforward. The detection images were still the NIC3 mosaics, and the object images were 2×2 binned ACS mosaics that were convolved by the PSF of the J_{110} images (derived using the TinyTim tool). The binning operation was sum, which preserves the original ACS magnitude zeropoints.

4. OVERDENSITY OF i -DROPOUTS

Using the newly produced ACS mosaics of Par1, new NIC3 data obtained at two pointings within Par1, and a new ACS parallel field Par2 for comparison, here we will re-examine the overdensity of i -dropouts in Par1 reported by YWC03.

4.1. Overdensity of i -dropouts in Par1

YWC03 reported 30 i -dropouts in Par1, whose z_{850} magnitudes range from 26.8 to 28.3 mag. Using the correct zeropoints, their true z_{850} -band magnitude range should be 25.3 to 26.8 mag (see §3.3). The corresponding cumulative surface density thus is ~ 2.7 per arcmin² to $z_{850} = 26.8$ mag. Taken at its face value, this number is 3–4 times higher than those in other deep, high galactic-latitude ACS fields, including the Hubble Ultra Deep Field (HUDF; Beckwith et al. 2006). The i -dropouts in YWC03 were selected based on their invisibility in the i_{775} image, i.e., by selecting sources that have $S/N \geq 5$ in z_{850} but have $S/N < 2$ in i_{775} . As a result, about 2/3 of those objects have $i_{775} - z_{850} > 2.0$ mag. Other studies utilizing ACS data (including YW04) all have adopted less stringent selection criterion of $i_{775} - z_{850} \geq 1.3$ mag or $i_{775} - z_{850} \geq 1.5$ mag. Therefore, the high surface density of YWC03 is even more difficult to be reconciled with all the other later work.

To study this problem in detail, here we reselect i -dropouts in Par1 from the new z_{850} -based ACS catalog as described in §3.3. We only consider sources with $S/N \geq 5$ in z_{850} , and adopt the color criterion of $i_{775} - z_{850} \geq 1.3$ mag for ease of comparison with other results. The candidates thus selected are visually examined to eliminate false detections such as residual cosmic rays and image defects. The final i -dropout sample consists of 356 objects to $z_{850} = 28.0$ mag. This is much deeper than what we achieved in YWC03, and is the result of the much improved data quality. In particular, 198 of them have $z_{850} \leq 26.8$ mag (among which 21 have $i_{775} - z_{850} \geq 2.0$ mag), which is a factor of 20 more than the i -dropouts selected in the HUDF (YW04; Bunker et al. 2004) to the same depth. This confirms – and reinforces – the unusually large overdensity of i -dropouts seen by YWC03. The distribution of these i -dropouts in Par1 are shown in Fig. 2.

A necessary condition for an i -dropout being a legitimate candidate of galaxy at $z \approx 6$ is that it must be a dropout in bluer bands. However, Par1 does not have any data to the blue of i_{775} . Fortunately, as a subset of these i -dropouts have NIC3 observations, we can use their ACS-to-NIC3 colors to judge whether they are consistent with being galaxies at $z \approx 6$.

4.2. Optical-to-IR colors of i -dropouts in Par1

In total, 21 i -dropouts are detected in our NIC3 data. Fig. 3 displays the image cut-outs of one such object. The optical-to-IR color-color diagrams of all these sources are shown in the left panel of Fig. 4. For comparison, the right panel of Fig. 4 shows the similar color-color diagrams from the HUDF.

It is clear that the i -dropouts in Par1 reside in the similar regions in the optical-to-IR color space as the i -dropouts in the HUDF. In particular, they are well separated from brown dwarf stars and E/S0 galaxies at lower redshifts, which are the most common contaminants to $z \approx 6$ galaxy samples selected by the drop-out technique.

4.3. A similar overdensity of i -dropouts in Par2

In order to compare with the results obtained in Par1, we perform i -dropout selection in Par2 in a similar way. As this field has g_{475} data, an additional constraint of non-detection in g_{475} at 2σ level is imposed for the selection. The final i -dropout sample consists of 20 objects to $z_{850} = 26.5$ mag, which, while much less than the ones in Par1, is still a factor of ~ 7 more than those found in the HUDF to the same depth; in other words, the overdensity of i -dropouts also seems to present in Par2.

5. ALTERNATIVE INTERPRETATION OF THE OVERDENSITY

The analysis in §4 indicates that the i -dropouts in Par1 are consistent with being galaxies at $z \approx 6$, and that the overdensity is also present in Par2. If this interpretation is true, we will have to draw the conclusion that the overdensity of i -dropouts in this region is due to an extremely unusual concentration of $z \approx 6$ galaxies over ~ 10 Mpc scale. In this section, however, we present another possibility.

5.1. Excess of field population in Par1 & Par2

The alternative interpretation is triggered by an unusual field population seen in both Par1 and Par2. This is illustrated in Fig. 5, which shows the z_{850} vs. $i_{775} - z_{850}$ color-magnitude diagrams in these fields using the z_{850} -based catalogs, together with the corresponding diagrams constructed in the HUDF based on the photometry from YW04. The left panel only plots the sources at $S/N > 5$, while the right panel includes all the sources at $S/N > 3$. A striking feature in this figure is the large concentration of objects at the faint end in the two parallel fields, which is not seen in the HUDF (and other deep ACS fields). Due to the shallower depth in Par2, this population is at the verge of being detectable at $S/N > 5$; however, it gets very prominent if the threshold is lowered to $S/N > 3$. YWC03 noticed only a hint of this excess in Par1; the source detection back then did not reach a sufficient depth that could unambiguously confirm its existence.

This excess of faint field objects in Par1 and Par2 is present in all passbands. To quantify this excess, Fig. 6 compares the surface densities of the detected sources in these two fields and the ones in the HUDF, derived at two different threshold levels of $S/N > 3$ (left panel) and $S/N > 5$ (right panel). Again, while the excess in Par2 is only detectable when the sources of low S/N are included, the excess in Par1 is obvious even at a high source detection threshold. This excess starts at about 26.0 mag in both Par1 and Par2, and extends to a much fainter level. In particular, the deep mosaics in Par1 allow this excess to be traced to at least ~ 28.2 and 27.2 mag in i_{775} and z_{850} , respectively. To further ensure the existence of the excess, we split the available images of Par1 into two groups and created shallower stacks in both bands. The same excess was detected as well.

The i -dropout surface densities are also superposed in Fig. 6. We point out that the i -dropout excess in the two parallel fields resides in the region where the field population excess happens. This is further discussed later in the paper.

5.2. Resolving diffuse light from interacting galaxy pair

What is the nature of this field population excess? The answer probably lies in the proximity of Par1 and Par2 to the galaxy pair M60/NGC4647, which is several arcminutes away to the South (see Fig. 1). Extended diffuse emissions of different natures have been detected around some nearby galaxies, for example in NGC 5907 (Shang et al. 1998; Zheng et al. 1999) and in M31 (e.g., Ferguson et al. 2002). While there is no previous report in the literature, we speculate that such extended diffuse emission also exists around M60/NGC4647, and propose that the excess population is due to the fact that we have resolved the diffuse light extending from this interacting pair. If we adopt an average distance of ~ 15.7 Mpc to M60/NGC4647 (from NASA/IPAC Extragalactic Database), Par1 and Par2 are ~ 32 and 69 kpc away from the center of pair, respectively. Therefore, what we have detected are most likely the halo stars of the two galaxies and/or the tidal “debris” repelled from this pair during the course of the interaction.

Here we exam the property of this excess more closely. We only use Par1 for this purpose, as the data in this field are much deeper than in Par2. Fig. 7 plots the surface densities of $S/N > 5$ sources in Par1 as functions of magnitudes in i_{775} (left) and z_{850} (right), and compares them with the results in the HUDF. The insets show the net excess after subtracting the surface density calculated in the HUDF. Tab. 1 lists the surface densities of the net excess as a function of magnitudes.

Taken at face value, the net excess in Par1 as shown in Fig. 7 has a total magnitude of 15.0 and 15.7 mag in i_{775} and z_{850} , respectively. The average surface brightness from the net excess (i.e., spreading the total integrated light of the net excess over the entire field of Par1), on the other hand, is 26.6 and 27.2 mag/arcsec² in i_{775} , and z_{850} , respectively. If this excess is isotropic with respect to M60/NGC4647, the total magnitude integrated over an annulus 3.4' in width (i.e., about the width of one ACS field) at the distance of Par1 (centering on the galaxy pair) is 12.2 mag in i_{775} and 12.9 mag in z_{850} . For comparison, the total flux of M60 in Johnson I-band

is 8.46 mag (or 0.925 Jy, i.e., 8.98 mag in AB) within 84" aperture (Boroson, Strom & Strom 1983). Therefore, the total diffuse light within this annulus is about a few percent of the central galaxies.

The net excess peaks at about 27.1 and 26.6 mag in i_{775} and z_{850} . If these objects are indeed at the distance of Virgo Cluster, these values correspond to absolute magnitudes of -3.9 and -4.4 mag, respectively, which are in the regime of giants/supergiants or low luminosity globular clusters.

We shall point out that the excess that we detected relates more closely to M60/NGC4546 rather than to the Virgo Cluster in general. A supporting evidence comes from the spatial gradient of this excess, which decreases in amplitude when moving away from the pair. This is demonstrated in Fig. 8, which plots the spatial distribution of all $S/N > 5$ sources at $z_{850} > 26.0$ mag detected in the z_{850} -based catalog of Par1. The gradient is obvious: there are more sources to the south, which is the direction where the galaxy pair lies.

Another piece of evidence is that the amplitude of this excess (see Fig. 7 and Tab. 1) cannot be attributed to the intracluster stellar populations of the Virgo Cluster alone. We only consider Virgo's intracluster globular clusters (IGC) and red giants (IRG), as they are the only two type of stellar objects that are within the luminosity range of the detected excess. The *total* contribution from Virgo's intracluster globular clusters (IGC) at > 26.0 mag, calculated using the Virgo's IGC surface density at the bright-end (e.g., Williams et al. 2007a; Cohen et al. 2003) and the symmetry of globular cluster luminosity function, is only ~ 0.3 – 3.0 arcmin⁻² (for any reasonable color transformation from F814W to F775W), depending on the proximity to a member galaxy. On the other hand, the deep *HST* surveys of Virgo's IRG (e.g., Ferguson, Tanvir & von Hippel 1998; Durrell et al. 2002; Williams et al. 2007b) show that their cumulative surface density to ~ 28.0 mag can be as high as ~ 110 arcmin⁻² (again for any reasonable F814W to F775W transformation). However, this is still a factor of 5–6 lower than what shown in Fig. 7 and Tab. 1.

5.3. Relation between i -dropout overdensity and field object overdensity

We suggest that the i -dropout overdensity observed in Par1 & Par2 might be related to the field object overdensity in the same regions. The field object excess becomes significant at 26.0 mag in both bands, and extends to at least 28.2 mag in i_{775} and 27.2 mag in z_{850} in the deeper Par1 images (see the insets in Fig. 8) where the excess can be traced to a faint level at high confidence. The i -dropouts selected in these fields resides in the z_{850} magnitude range that the field object excess spans (Fig. 6). The spatial distribution of the i -dropouts also seems to follow the gradient that seen in the distribution of the excess field population (see Fig. 2 & 7).

This excess field population is also red in color. Fig. 9 shows the surface densities of the sources in the above mentioned magnitude ranges as a function of $i_{775} - z_{850}$ color. For comparison, the surface densities of the HUDF sources in the same magnitude ranges are also shown. The insets plot the net excess using the HUDF result as the reference. The excess population peaks at

$i_{775}-z_{850} \approx 0.35$ mag in the i_{775} image, and peaks at $i_{775}-z_{850} \approx 0.60$ mag in the z_{850} image. Note that the distribution extends continuously beyond $i_{775}-z_{850} \geq 1.3$ mag, which is the regime where the i -dropouts are selected.

If the i -dropouts are indeed some stellar objects related to M60/NGC4647, what type of stars could they be? Thus far we have not yet been able to identify the satisfactory candidates. As Fig. 4 shows, brown dwarfs are not likely to contribute much to our i -dropout sample because their optical-to-IR colors are different. In addition, their luminosities are too low. The only possibility then left is dusty stellar population, for example, Asymptotic Giant Branch (AGB) stars. However, the optical-to-IR colors of AGB stars are quite different from the i -dropouts as well. This is illustrated in Fig. 10, where the synthesized colors of AGB stars generated from the model spectra of Lancon & Mouhcine (2002) are superposed on the color-color diagrams of the i -dropouts in Par1. We should also point out that no external dust extinction to any known types of stars could produce such colors; no known extinction law could create such a red color in $i_{775} - z_{850}$ and yet keep $z_{850} - J_{110}$ and $J_{110} - H_{160}$ colors around zero.

The red, excess field objects that we have discovered here seem to have some connection to the so-called ‘‘Red Halo Phenomenon’’ (Zackrisson et al. 2006), which refers to the very red colors of the halos found around some galaxies (e.g., Zibetti, White & Brinkmann 2004; Zibetti & Ferguson 2004; Taylor et al. 2005). Such red halos cannot be easily explained by standard stellar populations. The $i_{775} - z_{850}$ color shown in Fig. 9 quantitatively agrees with that of the halo around an edge-on disk galaxy in the HUDF reported by Zibetti & Ferguson (2004). Therefore, the excess field objects that we see might represent the first example where such red halos have been resolved, and the i -dropouts might be the most extreme sources among this population that is most difficult to explain.

6. SUMMARY

In this paper, we use new and existing *HST* data to closely examine the large overdensity of i -dropouts that YWC03 found in a deep ACS parallel field. The new data include NIC3 imaging of a subset of the i -dropouts, and a set of new ACS parallel data in a nearby region obtained during the NIC3 observations. We confirm that a factor of ~ 20 overdensity of i -dropouts does exist in the parallel field of YWC03, and that the optical-to-IR colors of these objects are similar to those selected in other deep ACS fields such as the HUDF.

However, these i -dropouts might *not* be galaxies at $z \approx 6$ as one would expect. During the course of our investigation, we have found a large excess of discrete sources in both the field of YWC03 and the new ACS parallel field. This excess is most likely due to a stellar population that is related to M60/NGC4647, an interacting galaxy pair in the Virgo Cluster, which lies several arcminutes to the south of the ACS parallel fields. At the distance of the Virgo Cluster, the ACS parallel fields are several tens of kpc away from the galaxy pair, and hence the stellar objects are likely tidal ‘‘debris’’ expelled from the pair and/or distant halo stars belong to these two galaxies. Both the spatial distribution and the amplitude of the excess indicate that it is a population related more closely to the galaxy pair rather than to the Virgo’s intracluster populations.

The i -dropouts in the field of YWC03 are within the magnitude range where the field object excess occurs. Their distribution also shows similar spatial gradient of the field object excess. Most importantly, the field object excess is red in color, and the red wing of its color distribution extends well into the regime where the i -dropouts were selected. For these reasons, we believe these i -dropouts are part of the stellar objects that constitute the field object excess rather than galaxies at $z \approx 6$.

Nevertheless, we should caution that we still cannot completely rule out the possibility that these i -dropouts might indeed be $z \approx 6$ galaxies. On one hand, we do not have any definite evidence against this interpretation. On the other hand, we have not yet found a stellar population that can reasonably explain the colors of these i -dropouts. To unambiguously identify their nature, spectroscopic observations of these objects are in demand. As the brightest sources in our sample are brighter than 26.0 mag in z_{850} , this might be feasible with the existing spectrographs at our current 8–10m class telescopes.

The authors thank the referee for the useful comments. We also thank Seth Cohen, Inese Ivans, Daisuke Kawata, Huub Röttgering and François Schweizer for helpful discussions. Support for program HST-GO-09780.* was provided by NASA through a grant from the Space Telescope Science Institute, which is operated by the Association of Universities for Research in Astronomy, Inc., under NASA contract NAS 5-26555. This research has made use of the NASA/IPAC Extragalactic Database (NED) which is operated by the Jet Propulsion Laboratory, California Institute of Technology, under contract with the National Aeronautics and Space Administration.

REFERENCES

- Beckwith, S. V. W., et al. 2006, *AJ*, 131, 1729
 Bertin, E. & Arnouts, S. 1996, *A&AS*, 117, 393
 Bouwens, R. J., et al. 2003, *ApJ*, 595, 589
 Bouwens, R. J., et al. 2004, *ApJ*, 606, L25
 Bruzual, A. G. & Charlot, S. 1993, *ApJ*, 405, 538
 Bunker, A. J., Stanway, E. R., Ellis, R. S., & McMahon, R. G. et al. 2004, *MNRAS*, 355, 374
 Cohen, S. H., et al. 2003, *AJ*, 125, 1762
 Dickinson, M., et al. 2004, *ApJ*, 600, L99
 Durrell, P. R., et al. 2002, *ApJ*, 570, 119
 Ferguson, A. M. N., et al. 2002, *AJ*, 124, 1452
 Ferguson, H. C., Tanvir, N. R. & von Hippel, T. 1998, *Nature*, 391, 29
 Ford, H., et al. 2003, in ‘‘Future EUV and UV Visible Space Astrophysics Missions and Instrumentation’’, eds. J. C. Blades & O.H. Siegmund, *Proc. SPIE*, Vol. 4854, 81
 Fruchter, A. S. & Hook, R. N. 2002, *PASP*, 114, 144
 Koekemoer, A. M., Fruchter, A. S., Hook, R. N., & Hack, W. 2002, in ‘‘The 2002 HST Calibration Workshop : Hubble after the Installation of the ACS and the NICMOS Cooling System’’, eds. Santiago Arribas, Anton Koekemoer, and Brad Whitmore, Baltimore, USA, p.337
 Lancon, A. & Mouhcine, M. 2002, *A&A*, 393, 167

- Madau, P. 1995, ApJ, 441, 18
Pavlovsky, C., et al. 2005, "ACS Data Handbook", Version 4.0, Baltimore: STScI.
Shang, Z., et al. 1998, ApJ, 504, L23
Somerville, R. S., et al. 2004, ApJ, 600, L171
Stanway, E. R., Bunker, A. J., & McMahon, R. G. 2003, MNRAS 342,439
Sparks, W. B., et al. 2001, ACS Default (Archival) Pure Parallel Program (ISR01-06)
Spergel, D. N., et al. 2003, ApJS, 148, 175
Spergel, D. N., et al. 2007, ApJS, 170, 377
Steidel, C. C. & Hamilton, D. 1992, AJ, 104, 941
Taylor, V. A., Jansen, R. A., Windhorst, R. A., Odewahn, S. C., & Hibbard, J. 2005, ApJ 630, 78
Williams, B. F., et al. 2007a, ApJ, 654, 835
Williams, B. F., et al. 2007b, ApJ, 656, 756
Yan, H., Windhorst, R. & Cohen, S. 2003, ApJ, 585, L93 (YWC03)
Yan, H. & Windhorst, R., 2004, ApJ, 600, L1 (YW04)
Zackrisson, E., et al. 2006, ApJ, 650, 812
Zheng, Z., et al. 1999, AJ, 117
Zibetti, S. & Ferguson, A. M. N., 2004, MNRAS, 352, L6
Zibetti, S., White, S. D. M & Brinkmann, J. 2004, MNRAS, 347, 556

TABLE 1
SURFACE DENSITY OF THE $S/N > 5$ SOURCE NET EXCESS
IN PAR1 AS A FUNCTION OF MAGNITUDE

magnitude	$\Sigma(i_{775})$ (arcmin $^{-2}$)	$\Sigma(z_{850})$ (arcmin $^{-2}$)
25.55	0.51	1.35
25.65	1.96	0.93
25.75	2.52	2.62
25.85	5.13	2.51
25.95	5.54	4.67
26.05	7.11	6.99
26.15	9.60	13.13
26.25	14.58	15.86
26.35	18.93	19.76
26.45	29.74	29.16
26.55	34.35	30.55
26.65	36.93	24.61
26.75	38.54	18.89
26.85	42.51	12.57
26.95	43.04	8.78
27.05	47.17	7.04
27.15	45.84	8.32
27.25	43.59	2.24
27.35	36.64	—
27.45	39.49	—
27.55	37.16	—
27.65	26.10	—
27.75	24.45	—
27.85	18.44	—
27.95	11.06	—
28.05	9.66	—
28.15	0.58	—

¹. The net excess is as shown in the insets in Fig. 7, which is calculated using the count in the HUDF as the reference.

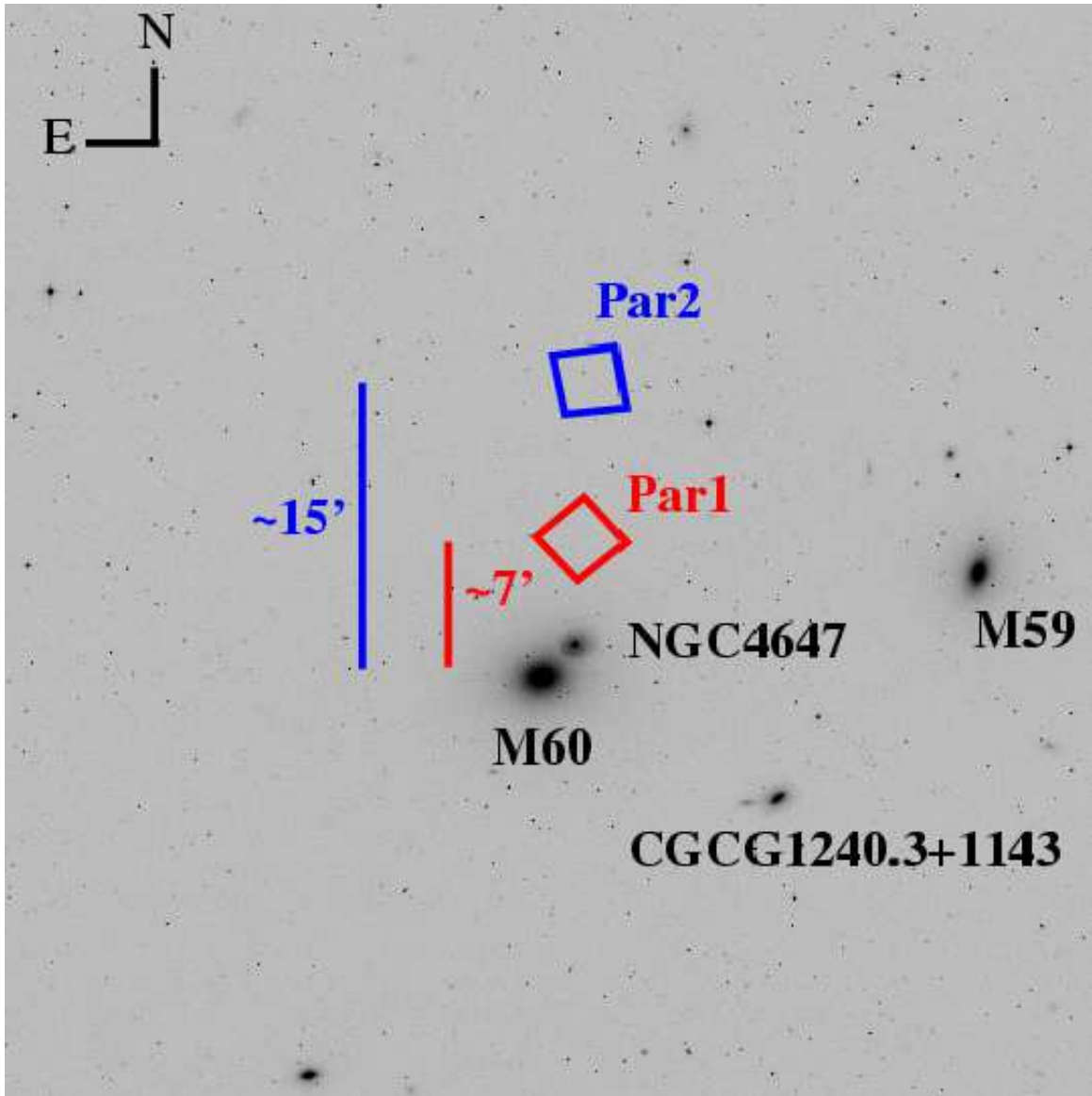


FIG. 1.— The locations of the fields studied in this work are shown on top of the image from the Digital Sky Survey. Both fields are several arcminutes away from the interacting galaxy pair, M60 & NGC4647, which are members of the Virgo Cluster. Par1 was taken in parallel mode by the ACS when the WFPC2 was observing NGC4647, while Par2 was taken by the ACS in parallel when NICMOS was observing two regions in Par1.

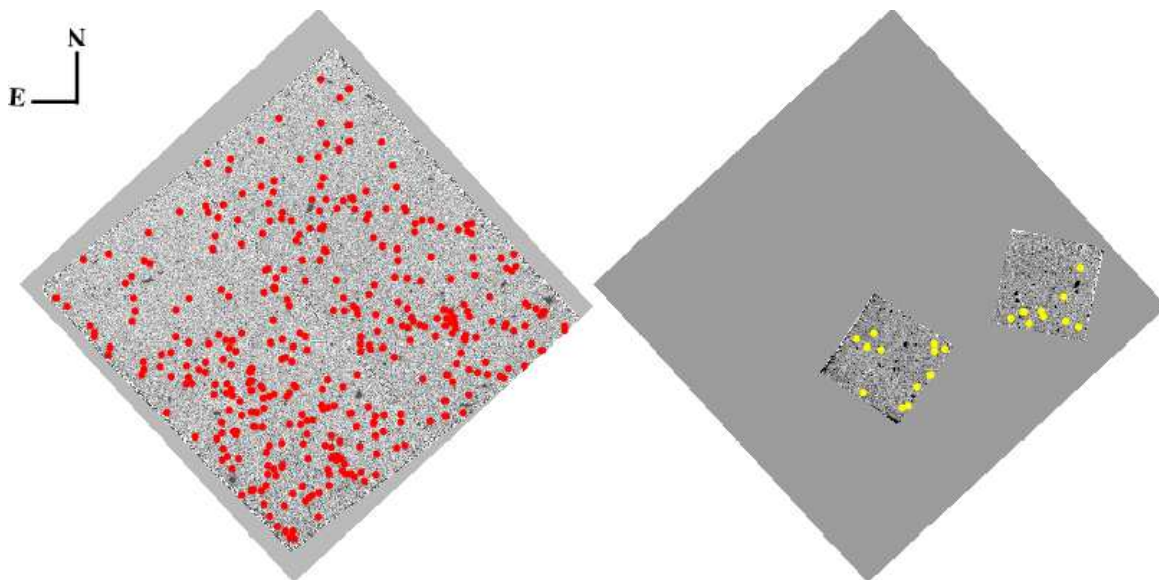


FIG. 2.— The left panel shows the locations of the i -dropouts in Par1 as red dots on top of the z_{850} -band mosaic of this field. The yellow dots in the right panel show the locations of the i -dropouts that are detected the NIC3 mosaic, which is the image in the background (note that the objects that are seemingly close to the edge are actually well within the region of good coverage).

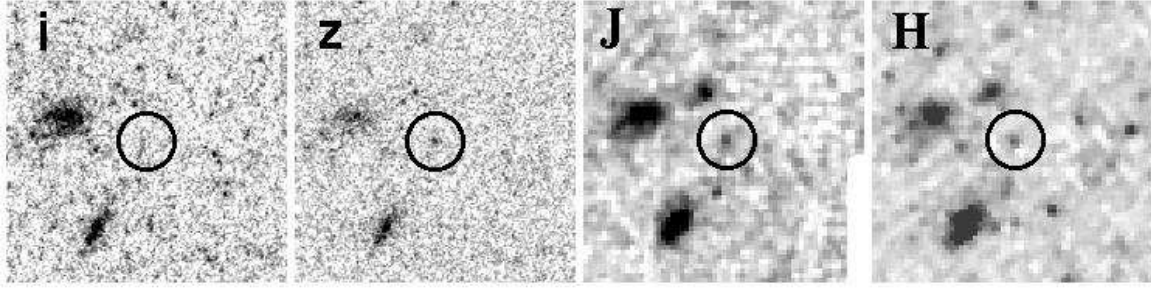


FIG. 3.— The image stamps of one i -dropout in our sample. The stamps are $6''$ on a side, and the circles in the middle are $0.2''$ in radius.

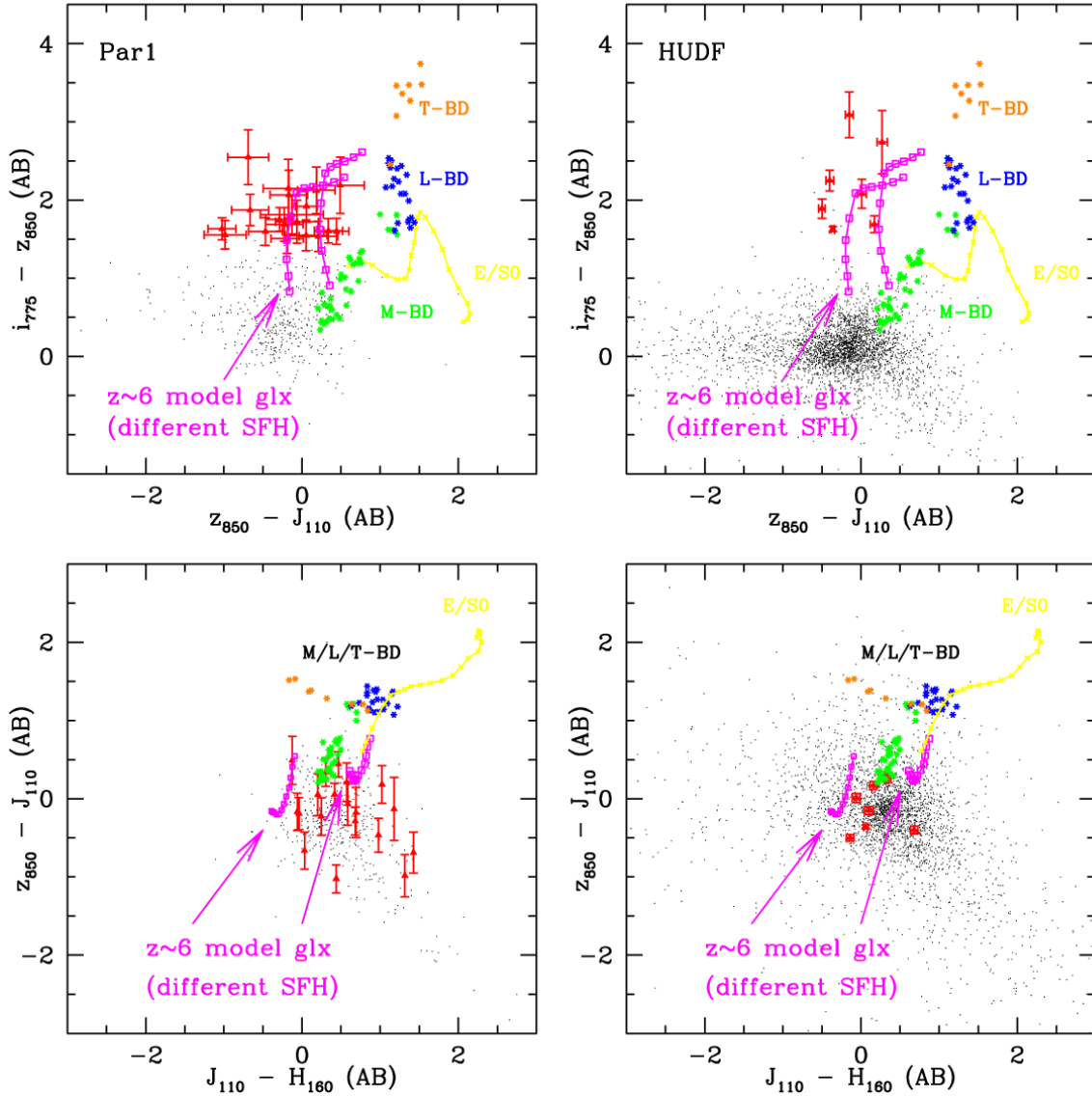


FIG. 4.— The optical-to-IR colors of the i -dropouts in Par1 (left) are compared with those of the i -dropouts in the HUDF (right). The i -dropouts are the red points with error bars, while the field objects are shown as the black dots. M-, L- and T-type brown dwarf stars are the green, blue and brown asterisks, respectively. The colors of E/S0 galaxy at $z = 1-3$ are shown as the yellow crosses. Two model galaxies at $5.5 \leq z \leq 6.5$, constructed using the models of Bruzual & Charlot (2003) of different star formation histories, are shown as the open magenta squares. The i -dropouts in Par1 occupy a similar region in the color space as do those in the HUDF.

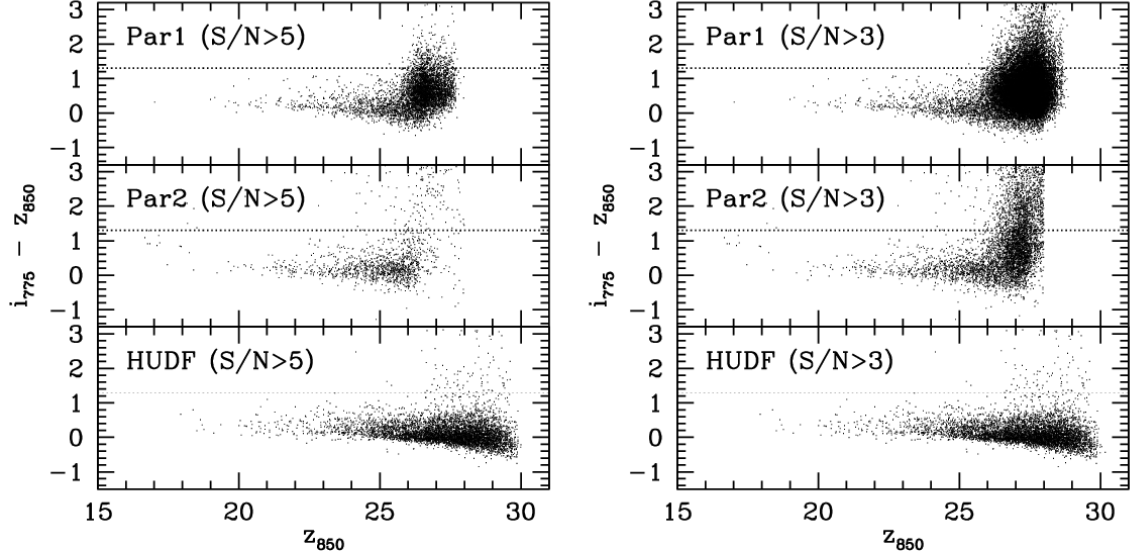


FIG. 5.— Comparison of the z_{850} vs. $i_{775}-z_{850}$ diagrams between the parallel fields and the HUDF. The objects plotted in the left panel are limited to the sources with $S/N > 5$, while those in the right panel are limited to the sources with $S/N > 3$. The dotted lines show the $i_{775}-z_{850} = 1.3$ color threshold above which the i -dropouts are selected. A unique feature in the two parallel fields is the large excess objects at the faint end, which is not seen in the HUDF. Due to its shallower depth, Par2 does not show this feature very clearly if only the sources at $S/N > 5$ are included; the excess becomes prominent when sources to $S/N = 3$ are included.

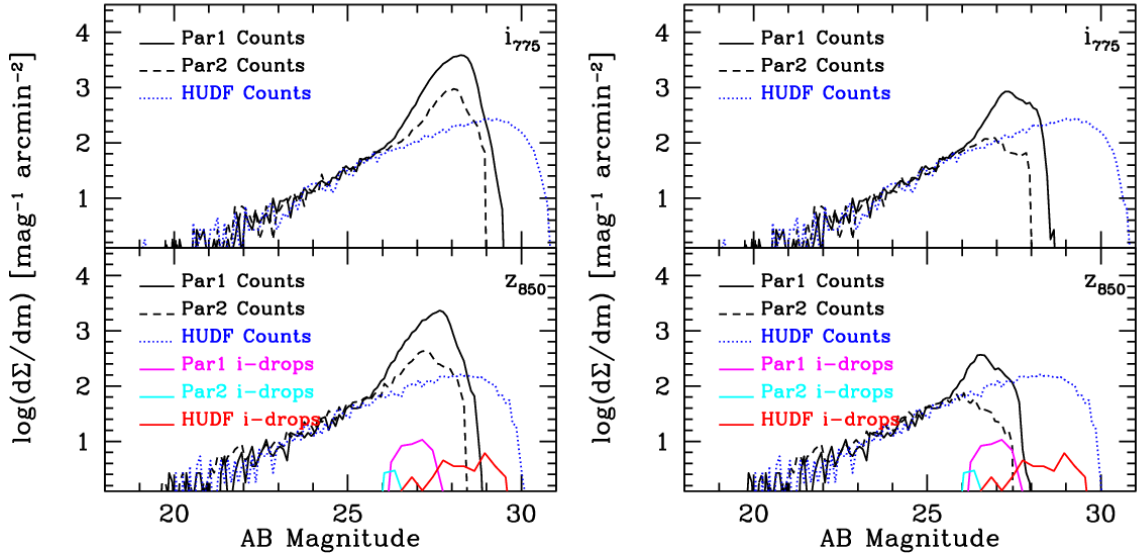


FIG. 6.— Comparison of the field source surface densities in the two parallel fields (solid and dashed black curves) and in the HUDF (blue dotted curves) at two threshold levels. The i_{775} -based catalogs are used for the statistics in i_{775} -band (top), while the z_{850} -based catalogs are used for the statistics in z_{850} -band (bottom). The left panel shows the statistics based on sources with $S/N > 3$, while the right panel shows the statistics based on sources with $S/N > 5$. The object excess in the two parallel fields is obvious. The surface densities of i -dropouts (all have $S/N > 5$ in z_{850}) in Par1, Par2 and HUDF are also shown as the magenta, cyan and red curves, respectively.

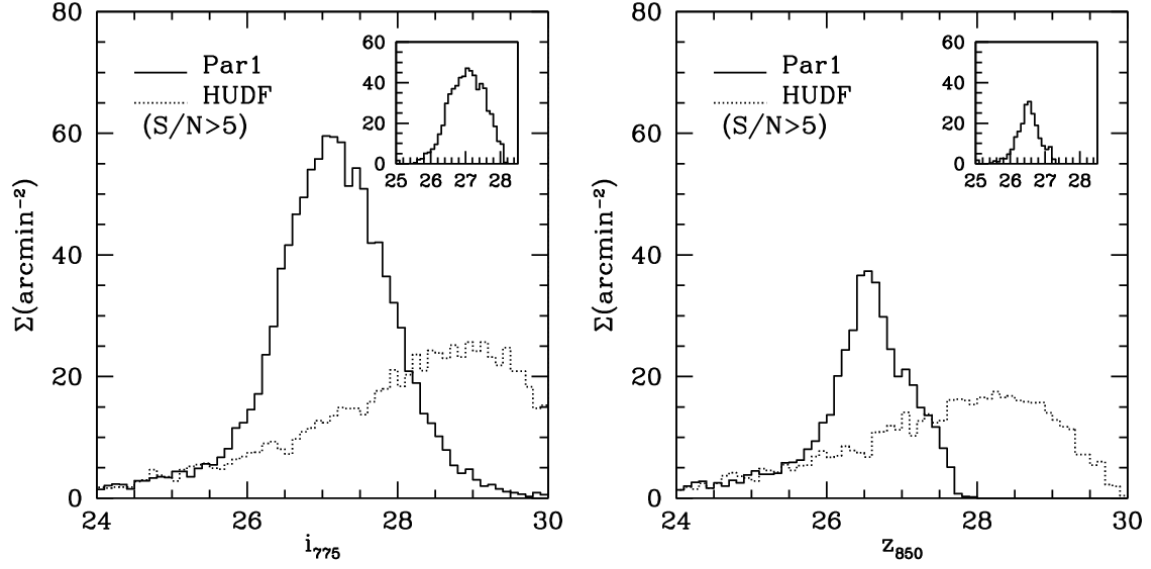


FIG. 7.— Field source excess of Par1 as a function of magnitude. The solid histograms are the surface densities in Par1, and the dotted histograms are those in the HUDF. The i_{775} -based catalogs are used for the figure in the left panel, while the z_{850} -based catalogs are used for the one in the right. Only sources at $S/N > 5$ are included for the statistics. The insets show the net excess using the HUDF as the reference. The excess extends to ~ 28.2 and 27.2 mag in i_{775} and z_{850} , respectively. The average surface brightness of the net excess corresponds to 26.6 and 27.2 mag/arcsec² in i_{775} , and z_{850} respectively. The total magnitudes of the net excess integrated over Par1 are $i_{775}=15.0$ and $z_{850}=15.7$ mag.



FIG. 8.— The spatial location of the excess field population has a clear gradient towards the direction of the interacting galaxy pair M60/NGC4647. This figure plots the positions of the z_{850} -based sources with $S/N > 5$ and $z_{850} > 26.0$ mag, which is the brightness level where the excess starts to be significant. North is up and East is to left. M60/NGC4647 is to the south of the field (see also Fig. 1). Note that the gap in the middle is caused by the gap between the two CCD chips of the ACS/WFC.

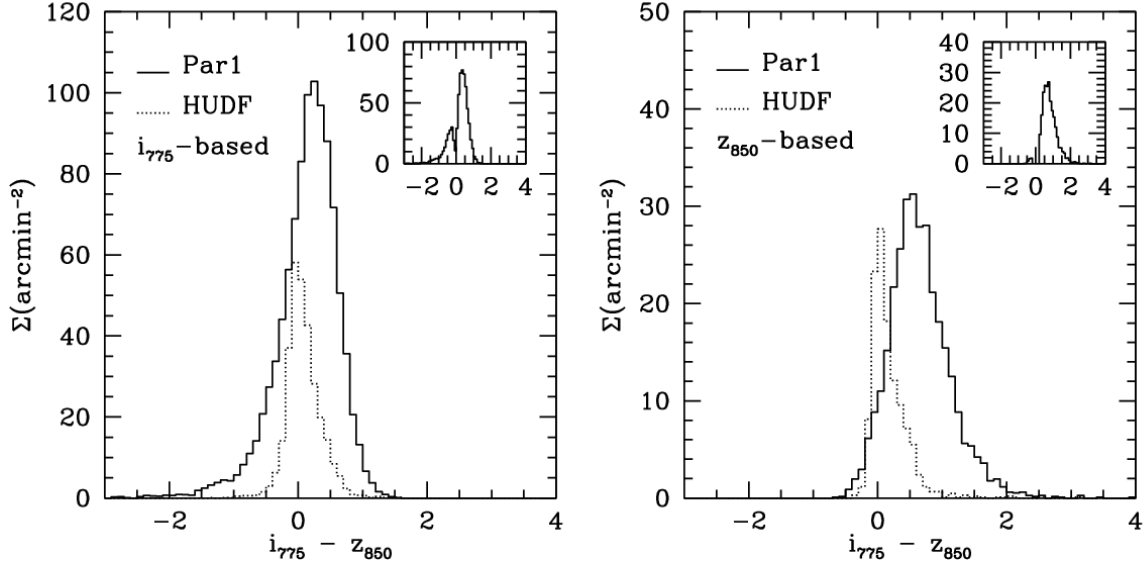


FIG. 9.— The excess population in the parallel fields is red in color. The solid histograms show the $i_{775}-z_{850}$ color distributions of Par1 sources that are within the magnitude ranges where the excess occurs, while the dotted histograms show the distribution of the HUDF sources within the same magnitude ranges. The insets show the distributions of the net excess using the HUDF as the reference. The i_{775} -based catalogs are used in the left panel, and the z_{850} -based catalogs are used in the right panel. The red wing of the excess population in z_{850} continuously extends to the regime where the i -dropouts are selected.

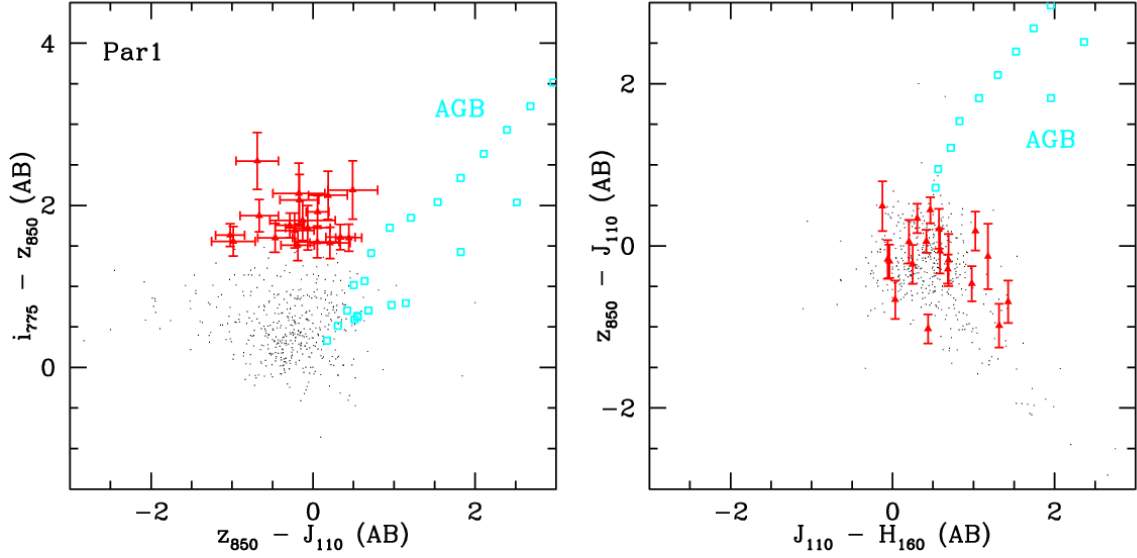


FIG. 10.— While the i -dropouts in the two parallel fields might well be part of the excess stellar population related to M60/NGC4647 instead of galaxies at $z \approx 6$, we have not yet been able to identify the type of stars that can create the colors of the i -dropouts. The most promising candidates are AGB stars, which have the necessary luminosities and are red in colors. However, AGB stars still cannot fully explain the colors of the i -dropouts. To illustrate this, the same color-color diagrams as in the left panel of Fig. 4 are shown here again, and the colors of AGB stars (cyan squares) from the models of Lancon & Mouchine (2002) are superposed. To avoid confusion, only the models that satisfy $i_{775} - z_{850} > 1.3$ mag are superposed in the right panel.